

Measurement Characterization and Autonomous Outlier Detection and Exclusion for Ground Vehicle Navigation With Cellular Signals

Mahdi Maaref and Zak M. Kassas^{ID}, *Senior Member, IEEE*

Abstract—An autonomous measurement outlier detection and exclusion framework for ground vehicle navigation using cellular signals is developed. The ground vehicle aids its onboard inertial measurement unit (IMU) with cellular signals in a tightly-coupled fashion in the absence of global navigation satellite system (GNSS) signals. First, cellular pseudoranges are characterized from an extensive wardriving campaign collected with a ground vehicle in different environments: open sky, urban, and deep urban. Then, a framework is developed, which accounts for outliers due to line-of-sight blockage and short multipath delays. These outliers induce biases in cellular pseudoranges and compromise the integrity of the navigation solution. Experimental results are presented evaluating the efficacy of the proposed framework on a ground vehicle navigating in the absence of GNSS signals. The results demonstrate the proposed framework detecting and excluding outliers, reducing the position root mean squared error (RMSE) by 41.5% and the maximum position error by 43.1%.

Index Terms—Outlier detection, cellular, RAIM, GNSS, IMU, navigation.

I. INTRODUCTION

GLOBAL navigation satellite system (GNSS) signals are insufficient for reliable and accurate ground vehicle navigation in deep urban environments due to the inherent weakness of their space-based signals. Hong Kong's dense urban environment, for instance, has less than 50% reliable GPS coverage [1]. What is more, GNSS signals are susceptible to malicious cyber attacks in the form of spoofing and jamming, which is particularly threatening as ground vehicles move towards semi- and full-autonomy [2].

Alternative sensing modalities to compensate for GNSS limitations and vulnerabilities have been the subject of extensive research recently. Such sensors include inertial measurement

Manuscript received June 21, 2019; revised November 15, 2019 and February 11, 2020; accepted April 8, 2020. Date of publication May 4, 2020; date of current version November 23, 2020. This work was supported in part by the National Science Foundation under Grants 1929571 and 1929965 and in part by the Office of Naval Research under Grants N00014-16-1-2809, and N00014-16-1-2305. (*Corresponding author: Zak M. Kassas.*)

The authors are with the Department of Mechanical and Aerospace Engineering, University of California, Irvine, CA 92697 USA (e-mail: mmaaref@uci.edu; zkassas@ieee.org).

This article has supplementary downloadable material available at <http://ieeexplore.ieee.org>, provided by the authors.

Color versions of one or more of the figures in this article are available online at <https://ieeexplore.ieee.org>.

Digital Object Identifier 10.1109/TIV.2020.2991947

units (IMUs) [3], lidars [4], cameras [5], radars [6], among others. Signals of opportunity represent another particularly fruitful class of sensing modalities [7]–[9]. Signals of opportunity are radio frequency signals that are not intended for navigation but can be exploited for navigation purposes, such as AM/FM radio signals [10], [11], digital television [12], [13], cellular [14], [15], Global System for Mobile Communications (GSM) [16], and low Earth orbit (LEO) satellites [17]. Among these signals, cellular signals are particularly attractive due to their (1) abundance in urban environments, (2) favorable geometric configuration by construction of the cellular infrastructure, (3) high received power due to their proximity, (4) transmission at various frequencies, and (5) high transmission bandwidth. These characteristics render them a reliable and accurate alternative navigation source, which is inherently more difficult to jam and spoof. Recent research results have demonstrated meter-level accurate navigation with cellular signals of opportunity with ground vehicles [18]–[21] and centimeter-level accurate navigation with aerial vehicles [22], [23].

In safety-critical applications, such as ground transportation and aviation, it is imperative to assess the integrity of the navigation solution. Integrity monitoring of GNSS signals and measurement outlier detection and exclusion have been extensively studied in the literature [24]–[26]. Among the different methods that have been developed to monitor GNSS signal integrity, receiver autonomous integrity monitoring (RAIM) inherently possesses desirable characteristics for ground-based receivers in urban canyons, due to RAIM's design flexibility and adaptability to urban environments [27]. In contrast to Satellite Based Augmentation System (SBAS) and Ground Based Augmentation System (GBAS) integrity methods, RAIM alleviates the need for costly, bulky, and computationally intensive infrastructure. RAIM detects GNSS pseudorange measurement outliers by only exploiting the redundancy of GNSS signals to check the measurements' consistency. RAIM can also be coupled with other sensing modalities to enhance the systems' integrity [28]. An initial work on integrity monitoring for cellular long-term evolution (LTE) signals-based navigation was conducted in [29], where the integrity of the LTE-based navigation solution and its corresponding protection levels (PLs) were studied. This paper extends [29] and makes two main contributions. First, outliers in received cellular LTE pseudorange measurements are characterized, namely biases due to line-of-sight (LOS) signal blockage and biases due to short multipath delays. Second,

an autonomous measurement outlier detection and exclusion approach is developed and validated numerically and experimentally.

This paper considers the following practical scenario. A ground vehicle is equipped with a GNSS receiver, an IMU, and a receiver capable of producing pseudoranges to multiple cellular LTE towers in the environment. The vehicle has initial access to GNSS signals, which are fused with the IMU measurements to estimate the vehicle's states (orientation, position, velocity, IMU biases, and GNSS receiver clock error). GNSS signals become unusable as the vehicle navigates in the environment (e.g., as it enters a deep urban canyon or in the presence of a malicious jamming attack on the GNSS frequency band). In the absence of IMU aiding with GNSS signals, the IMU errors grow unboundedly. However, cellular signals can be used as an IMU aiding source in the absence of GNSS signals to bound the IMU errors [30], [31]. Given the low elevation angle of cellular towers, cellular signals inevitably experience LOS blockage and suffer from multipath, which introduce unmodeled biases in the estimated pseudorange, rendering these pseudorange measurements outliers, which would contaminate the vehicle's estimated position, compromising the navigation system's integrity. This paper develops an autonomous outlier detection and exclusion framework for cellular LTE signals experiencing LOS blockage and multipath. The proposed framework assumes the position of the cellular towers to be known *a priori*. In addition, the proposed framework assumes the presence of a stationary agent in the vehicle's environment, referred to as the base, which has knowledge of its own state at all time. The base's purpose is to estimate the dynamic stochastic clock bias states of the cellular transmitters and to share these estimates with the navigating vehicle.

This navigating vehicle uses the cellular pseudoranges as an aiding source to correct the IMU's drift in the absence of GNSS signals. If the vehicle is equipped with other navigation sensors, adding pseudoranges from cellular towers via the framework discussed in this paper will further improve the navigation solution. The experimental results are presented validating the efficacy of the proposed method for a ground vehicle navigating in an urban environment (downtown Riverside, California, U.S.) over a trajectory of 1500 m. The experimental results show a reduction in the two-dimensional (2-D) root mean-squared error (RMSE) of 41.5% and the maximum 2-D error of 43.1% when measurement outliers were detected and excluded via the proposed method.

This paper is organized as follows. Section II describes the extended Kalman filter (EKF)-based navigation framework; including the vehicle's kinematics model, clock errors, cellular pseudorange measurements, estimation of the transmitter's clock bias states via the base, and estimation of the vehicle's states by fusing cellular pseudoranges and IMU measurements. Section III characterizes two main sources of errors that induce unmodeled biases in cellular pseudorange measurements: (i) LOS blockage and (ii) short multipath delays. It also formulates the autonomous outlier detection and exclusion framework. Section IV presents the experimental results evaluating the performance of the proposed framework on a ground vehicle

navigating in a deep urban environment without GNSS signals. Concluding remarks are given in Section V.

II. NAVIGATION FRAMEWORK

This section describes the ground vehicle navigation framework. The environment is assumed to comprise N_s terrestrial cellular transmitters, denoted $\{S_n\}_{n=1}^{N_s}$. It is assumed that the vehicle knows the location of the cellular transmitters (e.g., from a local or a cloud-hosted database). This database could be generated *a priori* via several approaches, such as radio mapping (e.g., [32], [33]) or satellite images. It is also assumed that the vehicle has an initial period of access to GNSS signals. During this period, the vehicle estimates its state and the cellular transmitters' clock bias states. After this period, it is assumed that GNSS signals become unusable, and the vehicle begins to navigate exclusively with cellular signals and its onboard IMU. The remainder of this section describes the vehicle-mounted receiver clock error dynamics, vehicle's kinematic model, and the EKF-based navigation framework. The EKF state space model is discussed in the following subsections.

A. Receiver Clock Error Dynamics Model and EKF Time Update

The receiver clock error state is given by

$$\mathbf{x}_{\text{clk},r} \triangleq \begin{bmatrix} c\delta t_r & c\dot{\delta}t_r \end{bmatrix}^T,$$

where c is the speed of light, δt_r is the receiver's clock bias, and $\dot{\delta}t_r$ is the receiver's clock drift. The vehicle-mounted receiver clock error state is assumed to evolve according to a double integrator driven by process noise $\tilde{\mathbf{w}}_{\text{clk},r} \triangleq [\tilde{w}_{\delta t,r}, \tilde{w}_{\dot{\delta}t,r}]^T$, whose elements are modeled as zero-mean, mutually independent noise processes and the power spectral density of $\tilde{\mathbf{w}}_{\text{clk},r}$ is given by $\tilde{\mathbf{Q}}_{\text{clk},r} = \text{diag}[S_{\tilde{w}_{\delta t,r}}, S_{\tilde{w}_{\dot{\delta}t,r}}]$ [34]. The discrete-time equivalent of the clock error dynamics can be expressed as

$$\mathbf{x}_{\text{clk},r}(k+1) = \Phi_{\text{clk}} \mathbf{x}_{\text{clk},r}(k) + \mathbf{w}_{\text{clk},r}(k), \quad \Phi_{\text{clk}} \triangleq \begin{bmatrix} 1 & T \\ 0 & 1 \end{bmatrix}, \quad (1)$$

where k is the measurement time-step, T is the sampling time, and $\mathbf{w}_{\text{clk},r}$ is the process noise, which is modeled as a zero-mean white random sequence with covariance

$$\mathbf{Q}_{\text{clk},r} = c^2 \begin{bmatrix} S_{\tilde{w}_{\delta t,r}} T + S_{\tilde{w}_{\dot{\delta}t,r}} \frac{T^3}{3} & S_{\tilde{w}_{\delta t,r}} \frac{T^2}{2} \\ S_{\tilde{w}_{\dot{\delta}t,r}} \frac{T^2}{2} & S_{\tilde{w}_{\dot{\delta}t,r}} T \end{bmatrix}. \quad (2)$$

Note that the power spectra $S_{\tilde{w}_{\delta t,r}}$ and $S_{\tilde{w}_{\dot{\delta}t,r}}$ can be related to the power spectral density of the fractional frequency deviation $y(t)$ of an oscillator from nominal frequency, which has the form $S_y(f) = \sum_{\alpha=-2}^2 h_\alpha f^\alpha$. A common approximation of $S_{\tilde{w}_{\delta t,r}}$ and $S_{\tilde{w}_{\dot{\delta}t,r}}$ is one that only considers the white frequency coefficient h_0 and the frequency random walk coefficient h_{-2} , specifically, $S_{\tilde{w}_{\delta t,r}} \approx \frac{h_0}{2}$ and $S_{\tilde{w}_{\dot{\delta}t,r}} \approx 2\pi^2 h_{-2}$ [35], [36].

Given the model in (1), the EKF time update can be readily calculated to yield the predicted state estimate $\hat{\mathbf{x}}_{\text{clk},r}(k+1|j)$, for $j \leq k$.

B. Vehicle Kinematics Model and EKF Time Update

The vehicle is assumed to be equipped with:

- an IMU and
- a receiver capable of producing pseudorange measurements to cellular transmitters (e.g., [13], [15], [20], [21], [37]).

If the vehicle is equipped with other navigation sensors (e.g., lidar, camera, etc.) the proposed framework could seamlessly integrate the outputs of these sensors to improve the vehicle's navigation solution. The vehicle's state vector \mathbf{x}_v is defined as

$$\mathbf{x}_v \triangleq \left[{}^I_G \bar{\mathbf{q}}^\top, {}^G \mathbf{r}_r^\top, {}^G \dot{\mathbf{r}}_r^\top, \mathbf{b}_g^\top, \mathbf{b}_a^\top \right]^\top,$$

where ${}^I_G \bar{\mathbf{q}}$ is the unit quaternion representing the vehicle's orientation (i.e., rotation from the global frame G to the IMU's inertial frame I); ${}^G \mathbf{r}_r \triangleq [x_r, y_r, z_r]^\top$ and ${}^G \dot{\mathbf{r}}_r$ are the 3-D position and velocity of the vehicle, respectively, expressed in G ; and \mathbf{b}_g and \mathbf{b}_a are the gyroscope and accelerometer biases, respectively. The detailed description of the vehicle kinematics model and EKF time update is presented in Appendix A. The EKF prediction error covariance time update is detailed in Appendix B.

C. EKF Measurement Model

After discretization and mild approximations, the pseudorange made by the vehicle-mounted receiver on the n -th cellular transmitter at the k -th time-step can be shown to be [38]

$$z_{s_n}(k) = \|{}^G \mathbf{r}_r(k) - \mathbf{r}_{s_n}\|_2 + c \cdot [\delta t_r(k) - \delta t_{s_n}(k)] + v_{s_n}(k), \quad (3)$$

where $\mathbf{r}_{s_n} \triangleq [x_{s_n}, y_{s_n}, z_{s_n}]^\top$ is the 3-D position of the n -th cellular transmitter, δt_{s_n} is the clock bias of the n -th cellular transmitter, and v_{s_n} is the measurement noise, which is modeled as a discrete-time zero-mean white Gaussian sequence with variance $\sigma_{s_n}^2$. The clock bias states of the cellular transmitters $\{\delta t_{s_n}\}_{n=1}^{N_s}$ are assumed to be known to the navigating vehicle through a base receiver as discussed the next subsection.

1) *Cellular Transmitter Clock Bias Estimation:* It is assumed that a base receiver is deployed in the same cellular environment of the navigating vehicle. While the vehicle could be located between the buildings, where GNSS signals are severely attenuated, the base receiver could be deployed on top of a building; therefore, it has access to unobstructed GNSS signals from which it can estimate its own clock bias. Hence, it is practical to assume that the base has complete knowledge of its position \mathbf{r}_B and its clock bias $c\delta t_B(k)$ for all k (e.g., from GNSS measurements). The base is making the following pseudorange measurements to the n -th cellular transmitter in the vehicle's environment

$$z_{B,s_n}(k) = \|\mathbf{r}_B - \mathbf{r}_{s_n}\|_2 + c \cdot [\delta t_B(k) - \delta t_{s_n}(k)] + v_{B,s_n}(k), \quad (4)$$

where v_{B,s_n} is the measurement noise, which is modeled as a zero-mean white Gaussian random sequence with variance σ_{B,s_n}^2 . Since \mathbf{r}_{s_n} , \mathbf{r}_B , and $c\delta t_B(k)$ are known, define the new measurement

$$\begin{aligned} z'_{B,s_n}(k) &\triangleq \|\mathbf{r}_B - \mathbf{r}_{s_n}\|_2 + c\delta t_B(k) - z_{B,s_n}(k) \\ &= c\delta t_{s_n}(k) - v_{B,s_n}(k). \end{aligned} \quad (5)$$

The base feeds the measurements z'_{B,s_n} defined in (5) into a Kalman filter (KF) to produce an estimate of $\mathbf{x}_{\text{clk},s_n} \triangleq [c\delta t_{s_n}, \dot{c\delta t}_{s_n}]^\top$, where $\dot{c\delta t}_{s_n}$ is the clock drift of the n -th cellular transmitter. The dynamics of $\mathbf{x}_{\text{clk},s_n}$ are the same as the ones of $\mathbf{x}_{\text{clk},r}$ defined in (1), except that $S_{\tilde{w}_{\delta t,r}}$ and $S_{\tilde{w}_{\delta t,s_n}}$ are now replaced with the n -th cellular transmitter-specific process noise power spectra, i.e., $S_{\tilde{w}_{\delta t,s_n}}$ and $S_{\tilde{w}_{\delta t,s_n}}$, respectively. Denote $\hat{c\delta t}_{s_n}(k|k)$ as the KF's n -th cellular transmitter clock bias estimate, $c\tilde{\delta t}_{s_n}(k|k) \triangleq c\delta t_{s_n}(k) - \hat{c\delta t}_{s_n}(k|k)$ as the estimate error, and $\sigma_{c\delta t_{s_n}}^2(k|k)$ as its estimation error variance.

2) *Pseudorange Measurement Model Used in the EKF:* The estimate of the cellular tower clock bias states produced by the base are sent to the navigating vehicle. Therefore, the pseudorange made by the vehicle-mounted receiver on the n -th cellular transmitter can be re-expressed as

$$\begin{aligned} z_{s_n}(k) &= \|{}^G \mathbf{r}_r(k) - \mathbf{r}_{s_n}\|_2 + c \cdot [\delta t_r(k) - \hat{c\delta t}_{s_n}(k|k)] \\ &\quad + v'_{s_n}(k), \end{aligned} \quad (6)$$

where $v'_{s_n}(k) \triangleq v_{s_n}(k) - \tilde{c\delta t}_{s_n}(k|k)$, which is the overall measurement noise with zero-mean and variance $\sigma_{v',s_n}^2 = \sigma_{s_n}^2 + \sigma_{c\delta t_{s_n}}^2$. The vector of pseudorange measurements to all N_s cellular transmitters is given by $\mathbf{z} = [z_{s_1}, \dots, z_{s_{N_s}}]^\top$ and it is assumed that the measurement noise $\{v'_{s_n}\}_{n=1}^{N_s}$ are independent.

D. EKF State and Covariance Measurement Update

The EKF's state measurement update $\hat{\mathbf{x}}(k+1|k+1)$ and associated estimation error covariance $\mathbf{P}(k+1|k+1)$ are computed using standard EKF update equations [35], except for the orientation state which is updated according to the quaternion error model [39]. The corresponding measurement Jacobian \mathbf{H} is given by

$$\mathbf{H} = [\mathbf{H}_v, \mathbf{H}_{\text{clk}}],$$

where,

$$\begin{aligned} \mathbf{H}_v &\triangleq \begin{bmatrix} \mathbf{0}_{1 \times 3} & \mathbf{1}_{s_1}^\top & \mathbf{0}_{1 \times 9} \\ \vdots & \vdots & \vdots \\ \mathbf{0}_{1 \times 3} & \mathbf{1}_{s_{N_s}}^\top & \mathbf{0}_{1 \times 9} \end{bmatrix}, \\ \mathbf{1}_{s_n} &\triangleq \frac{{}^G \hat{\mathbf{r}}_r(k+1|j) - \mathbf{r}_{s_n}}{\|{}^G \hat{\mathbf{r}}_r(k+1|j) - \mathbf{r}_{s_n}\|_2}, \end{aligned}$$

$$\mathbf{H}_{\text{clk}} \triangleq [\mathbf{h}_{\text{clk}} \quad \dots \quad \mathbf{h}_{\text{clk}}]^\top, \quad \mathbf{h}_{\text{clk}} \triangleq [1 \ 0]^\top.$$

The measurement noise covariance takes the form

$$\mathbf{R} = \text{diag} \left[\sigma_{v',s_1}^2, \dots, \sigma_{v',s_{N_s}}^2 \right].$$

III. OUTLIER CHARACTERIZATION AND DETECTION

This section analyzes cellular pseudorange measurements with and without outliers, leading to a characterization of the measurements accuracy and availability, which are formally defined as

- *Accuracy:* the degree of conformance of the measurements with the true ranges.

TABLE I
CHARACTERISTICS OF RECORDED CELLULAR SIGNALS

Environment	N_s	Freq. [MHz]	Bandwidth [MHz]	Date [DD/MM/YYYY]	Traversed path [m]
Open sky	2	2125, 1955	20	13/5/2019	Stationary receiver
Semi-urban and urban	2	2145, 1955	20	15/11/2016	1500
	3	2145, 1955	20	20/1/2017	2000
	4	2145, 739	20, 10	22/6/2018	1600
	5	1955, 739	20, 10	27/6/2016	580
	3	739	10	5/11/2017	825
	5	1955, 739	20, 10	22/8/2018	1800
Deep urban	2	2145, 1955	20	12/10/2018	345
	2	2145, 1955	20	24/8/2018	500

- *Availability:* the percentage of time that the measurements are usable by the navigator [40].

While GNSS ranging performance has been the subject of many studies [41], [42], this is not the case for ranging with cellular signals. Without such understanding, one cannot rigorously define what constitutes an outlier in cellular pseudorange measurements. The next subsection studies cellular pseudorange measurements collected over hours of driving in different environments, leading to a statistical model of their accuracy. Next, outliers in cellular pseudoranges are analyzed in terms of biases due to LOS blockage and short multipath delays. Finally an outlier detection test is formulated.

A. Cellular Pseudorange Measurements Characterization

To analyze the accuracy of cellular LTE pseudorange measurements, a ground vehicle was driven for several hours in different environments: semi-urban, urban, and deep urban. For comparison purposes, pseudorange measurements from an antenna placed on the roof of the Engineering Gateway building at the University of California, Irvine were collected over 250 seconds to resemble an open sky environment. Received LTE signals from different LTE towers corresponding to different U.S. cellular providers transmitting at different frequencies and different cell-specific reference signal (CRS) bandwidths were collected, from which pseudorange measurements were obtained. The pseudoranges were obtained using the Multichannel Adaptive TRansceiver Information eXtractor (MATRIX) software-defined receiver (SDR) discussed in [20], [21]. Table I summarizes the characteristics of recorded cellular signals.

Next, the collected pseudorange measurements were compared against the true ranges to characterize the pseudorange measurement errors. Recall from (3) that the pseudorange is composed of three terms: (i) true range between the receiver and the transmitter (namely, $\|{}^G\mathbf{r}_r(k) - \mathbf{r}_{s_n}(k)\|_2$), (ii) an error term due to the difference between the clock bias of the receiver and the transmitter (namely, $c\Delta\delta t_{r,s_n}(k) \triangleq c \cdot [\delta t_r(k) - \delta t_{s_n}(k)]$), and (iii) an error term due to measurement noise (namely, $v_{s_n}(k)$).

To evaluate the statistics of the measurement noise term, $v_{s_n}(k)$, the true range between the receiver and the transmitter can be readily removed from knowledge of the cellular transmitters' location and the receiver's ground truth position (which is obtained from a GNSS receiver), i.e.,

$$\begin{aligned} z'_{s_n}(k) &\triangleq z_{s_n}(k) - \|{}^G\mathbf{r}_r(k) - \mathbf{r}_{s_n}(k)\|_2 \\ &= c\Delta\delta t_{r,s_n}(k) + v_{s_n}(k). \end{aligned}$$

Next, the clock error term $c\Delta\delta t_{r,s_n}(k)$ must be removed. In GNSS, the satellites' clock biases are transmitted in the navigation message and can be removed by the receiver from the pseudorange measurements. To reduce the receiver's clock bias and drift issues, an atomic clock can be used [43]. Removing the effect of clock biases to evaluate the empirical measurement error of LTE pseudoranges is a more challenging problem. On one hand, the LTE transmitters' clock biases, which are typically relatively stable [44] (e.g., using a GPS-disciplined oscillator (GPSDO)), are unknown to the receiver. On the other hand, the measured pseudoranges are produced by a receiver which does not possess a clock of atomic stability.

To remove $c\Delta\delta t_{r,s_n}(k)$ from $z'_{s_n}(k)$, it is assumed that this term evolves according to a first-order polynomial model with a constant initial clock bias $c\dot{\delta}t_{r,s_n,0}$ and drift $c\ddot{\delta}t_{r,s_n,0}$ [45], i.e.,

$$c\Delta\delta t_{r,s_n}(k) = c\dot{\delta}t_{r,s_n,0} kT + c\ddot{\delta}t_{r,s_n,0} + \eta_{r,s_n}(k), \quad (7)$$

where $\eta_{r,s_n}(k)$ is a random sequence which models the mismatch between the true time evolution of $c\Delta\delta t_{r,s_n}(k)$ and the first-order polynomial approximation (7).

The constants $c\dot{\delta}t_{r,s_n,0}$ and $c\ddot{\delta}t_{r,s_n,0}$ can be estimated via least-squares by post-processing the recorded data $z'_{s_n}(k)$. It is important to note that this is a conservative approach to characterize the pseudorange measurement error, as this approach calculates the term $\check{v}_{s_n}(k) \triangleq v_{s_n}(k) + \eta_{r,s_n}(k)$, which is larger than the true measurement error $v_{s_n}(k)$.

To analyze the accuracy of the pseudorange measurement error, the statistics of the term $\check{v}_{s_n}(k)$ will be characterized. Fig. 1(a) shows $z'_{s_n}(k)$ for one of the towers from the open sky recorded signals. The constants $c\dot{\delta}t_{r,s_n,0}$ and $c\ddot{\delta}t_{r,s_n,0}$ are estimated from $z'_{s_n}(k)$ via least-squares and then subtracted from $z'_{s_n}(k)$ to get

$$z''_{s_n}(k) \triangleq z'_{s_n}(k) - [c\dot{\delta}t_{r,s_n,0} kT + c\ddot{\delta}t_{r,s_n,0}] = \check{v}_{s_n}(k).$$

Fig. 1(b) shows $z''_{s_n}(k)$ and Fig. 1(c)–(d) show the autocorrelation function (acf) and power spectral density (psd) of $z''_{s_n}(k)$, from which it can be seen that the term $\check{v}_{s_n}(k)$ is nearly white.

Therefore, if the receiver's or transmitter's clock type is unknown (i.e., the error component $\eta_{r,s_n}(k)$ cannot be modeled), the conservative term $z''_{s_n}(k)$ can be studied to characterize the pseudorange measurement error statistics.

In the case that both the receiver's and transmitter's clock types are known, the mismatch between the true time evolution of $c\Delta\delta t_{r,s_n}(k)$ and its first-order polynomial approximation, $\eta_{r,s_n}(k)$, can be characterized as follows. Using (1), the discrete-time equivalent dynamics model of the receiver and the

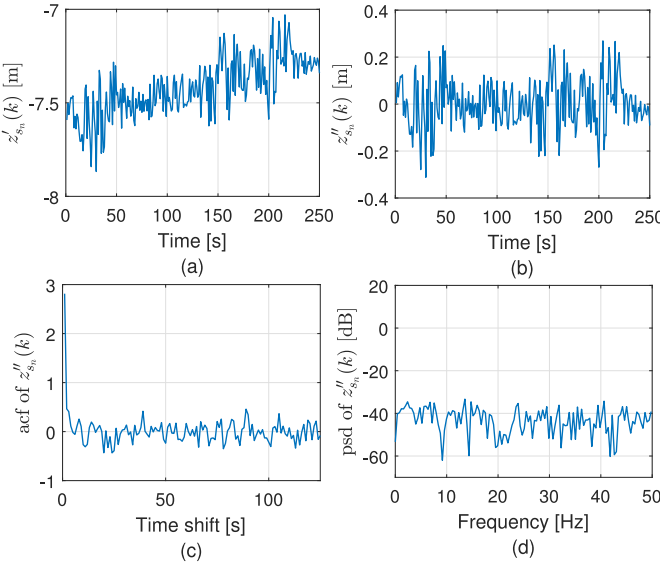


Fig. 1. Cellular pseudorange measurement error characterization. (a) Pseudorange measurement after subtracting the true range between the receiver and the transmitter, which is denoted as $z'_{sn}(k)$. (b) Resulting measurement after subtracting the clock bias difference between the receiver and the transmitter, which is denoted as $z''_{sn}(k)$. (c) The acf and (d) psd of $z''_{sn}(k)$ with a sampling frequency of 100 Hz.

transmitter clock error difference can be expressed as

$$\Delta \mathbf{x}_{\text{clk},r,s_n}(k+1) = \Phi_{\text{clk}} \Delta \mathbf{x}_{\text{clk},r,s_n}(k) + \mathbf{w}_{\text{clk},r,s_n}(k), \quad (8)$$

where $\Delta \mathbf{x}_{\text{clk},r,s_n} \triangleq [c\Delta\delta t_{r,s_n}, c\Delta\dot{\delta}t_{r,s_n}]^\top$, $c\Delta\dot{\delta}t_{r,s_n}(k) \triangleq c \cdot [\dot{\delta}t_r(k) - \dot{\delta}t_{s_n}(k)]$ is the difference between the clock drift of the receiver and the transmitter, and $\mathbf{w}_{\text{clk},r,s_n} \triangleq [w_{\delta t_{r,s_n}}, w_{\dot{\delta}t_{r,s_n}}]^\top$ is the process noise, which is modeled as zero-mean white random sequence with covariance

$$\mathbf{Q}_{\text{clk},r,s_n} = \mathbf{Q}_{\text{clk},r} + \mathbf{Q}_{\text{clk},s_n},$$

where $\mathbf{Q}_{\text{clk},r}$ is obtained from (2). Recall that $\mathbf{Q}_{\text{clk},s_n}$ has the same form as $\mathbf{Q}_{\text{clk},r}$, except that $S_{\tilde{\omega}_{\delta t,r}}$ and $S_{\tilde{\omega}_{\dot{\delta}t,r}}$ are now replaced by the transmitter-specific spectra $S_{\tilde{\omega}_{\delta t,s_n}}$ and $S_{\tilde{\omega}_{\dot{\delta}t,s_n}}$, respectively. It is shown in Appendix C that $\eta_{r,s_n}(k)$ is a zero-mean white random sequence with variance σ_{η,r,s_n}^2 and is obtained from the k -th element of the vector

$$\eta_{r,s_n} = \mathbf{G}\mathbf{F}_1\mathbf{w}_1 + \mathbf{G}\mathbf{F}_2\mathbf{w}_2, \quad (9)$$

where \mathbf{G} , \mathbf{F}_1 , and \mathbf{F}_2 are deterministic matrices and

$$\mathbf{w}_1 \triangleq [w_{\delta t_{r,s_n}}(0), \dots, w_{\delta t_{r,s_n}}(K-2)]^\top$$

$$\mathbf{w}_2 \triangleq [w_{\dot{\delta}t_{r,s_n}}(0), \dots, w_{\dot{\delta}t_{r,s_n}}(K-3)]^\top,$$

where K is the number of total processed samples. The derivation of σ_{η,r,s_n}^2 , \mathbf{G} , \mathbf{F}_1 , and \mathbf{F}_2 are presented in Appendix C. Fig. 2 shows σ_{η,r,s_n} for a transmitter equipped with a high-quality oven-controlled crystal oscillator (OCXO) and four different receivers: (i) a receiver equipped with a high-quality OCXO, (ii) a receiver equipped with a typical OCXO, a receiver equipped with a typical temperature-compensated crystal

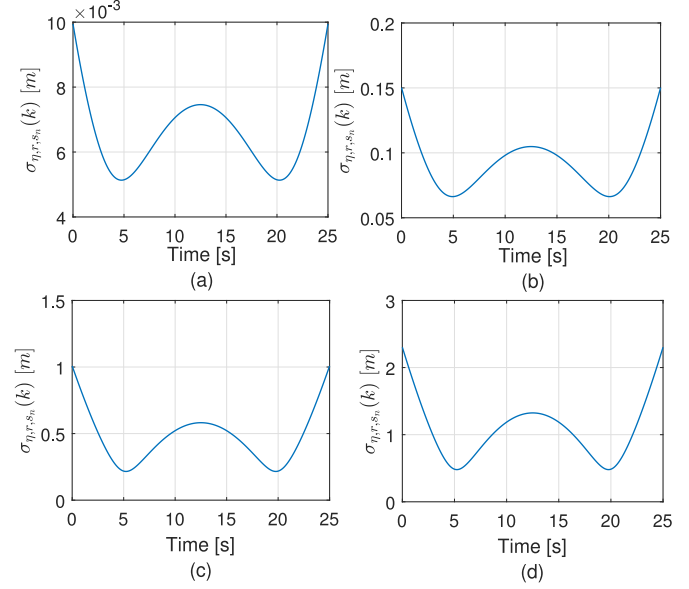


Fig. 2. The standard deviation $\{\sigma_{\eta,r,s_n}(k)\}_{k=0}^{K-1}$ of the vector η_{r,s_n} for four receivers, equipped with different oscillators: (a) high-quality OCXO, (b) typical OCXO, (c) typical TCXO, and (d) worst TCXO. Here, $K = 2,500$ samples and $T = 0.01$ s.

TABLE II
ML PARAMETERS OF GAUSSIAN PDFS OF PSEUDORANGE MEASUREMENT ERROR IN DIFFERENT ENVIRONMENTS

Environment	μ	σ
Open sky	1.14×10^{-15} m	0.11 m
Urban and semi-urban	-1.24×10^{-16} m	2.74 m
Deep urban	-1.05×10^{-15} m	5.42 m

oscillator (TCXO), and (iv) a receiver equipped with a worst TCXO. From Fig. 2, one can see the conservativeness of the mismatch $\eta_{r,s_n}(k)$ due to different clock types. In particular, the “inflation” in the calculated standard deviation of $\tilde{v}_{s_n}(k)$ compared to the standard deviation of $v_{s_n}(k)$ range between about one centimeter for (a) and about 2 m for (d). Fig. 3(a) illustrates the different environments in which the measurements were collected and Fig. 3(b) shows the empirical probability density functions (pdfs) found from the collected measurements. Overlaid on these pdfs are the maximum likelihood (ML) pdfs of a Gaussian. Table II summarizes the ML parameters of these pdfs, namely the mean μ and standard deviation σ , in different environment.

It is worth comparing the values in Table II to GPS measurement’s user range error (URE), which are shown to have a standard deviation of around 6 m [43].

B. Outlier Characterization

This subsection characterizes two sources of pseudorange measurement outliers: (i) bias due to LOS signal blockage where the non-LOS (NLOS) peak dominates and (ii) bias due to short

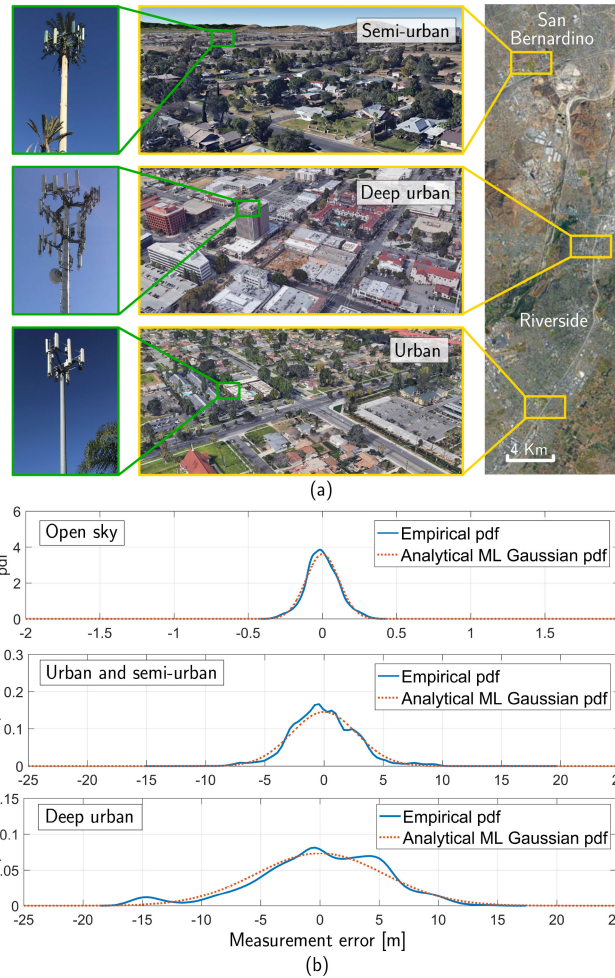


Fig. 3. Characterization of cellular pseudorange measurement accuracy in different environments. (a) Three environments: semi-urban, urban, and deep urban in which a ground vehicle was driven while collecting cellular signals. A zoom on some cellular towers from which the signals were collected is displayed. (b) Empirical pdf of pseudorange errors and analytical ML Gaussian pdfs for the environments in (a). In addition to these environments, the results corresponding to the stationary antenna in an open sky environment is shown.

multipath delay where the LOS peak and multipath peaks are indiscernible.

1) *Bias Due to LOS Signal Blockage:* In deep urban canyons, high-rise structures could completely block or significantly attenuate LOS signals from cellular transmitters. What is more dangerous is that these signals could be reflected off nearby objects, resulting in received multipath components with significantly higher power than the LOS signal. In these instances, it is imperative that the receiver continues to track the weak LOS signal instead of the non-LOS multipath in order to produce pseudorange measurements that are consistent with the model (3). Several approaches have been proposed to dynamically tune the LOS peak detection threshold in the presence of severe multipath [20], [46]. While these approaches have shown better performance compared to constant threshold approaches, they may fail to detect the LOS peak altogether when it has significantly less power than the multipath components. In this case, a large bias will be introduced in the pseudorange measurement.

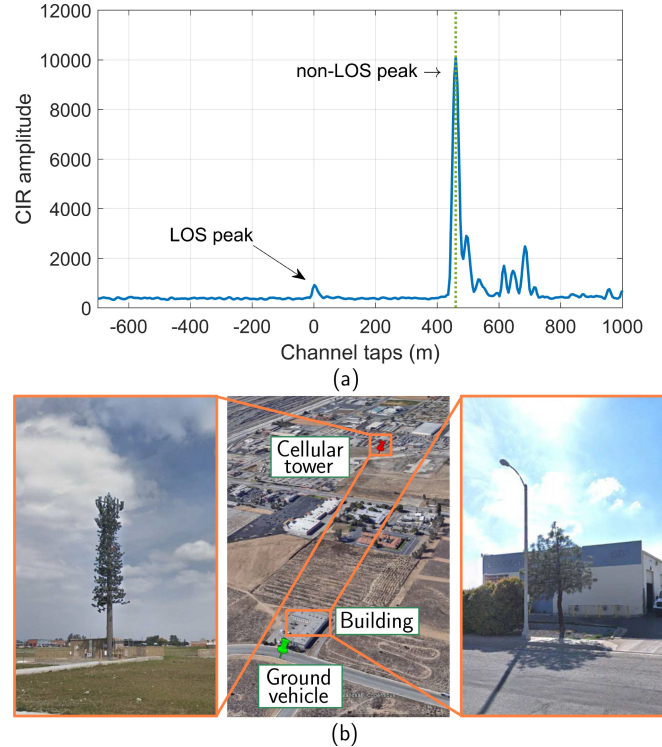


Fig. 4. An instance of the estimated CIR of real LTE signals passing through a building. (a): The LOS component which has a significantly lower amplitude than the multipath components. (b): The location of the cellular transmitter, the ground vehicle, and the building that significantly attenuates LOS signals in this instance.

This bias will contaminate the estimate, introducing tens of meters of errors in the estimated position [47]. Fig. 4 shows an instance of the estimated channel impulse response (CIR) from real LTE signals passing through a building. It can be seen that the power of the LOS component is significantly lower than that of the multipath component, which is at a path delay of approximately 440 m. This will introduce a large unmodeled bias in the pseudorange measurement. The objective of the outlier detection and exclusion approach discussed in Section III-C is to autonomously detect the presence of such bias and subsequently exclude the biased pseudorange measurement from the EKF calculations.

2) *Bias Due to Short Multipath Delays:* In the case of short multipath delays, i.e., the LOS peak is indiscernible from other multipath peaks, biases will be induced in the pseudorange measured by the receiver. This bias is characterized next. The true CIR for the i -th LTE symbol is given by

$$h_i(\tau) = \sum_{l=0}^{L-1} a_i(l) \delta(\tau - \tau_i(l)),$$

where L is the number of path delays, a_i corresponds to the complex-valued amplitude, and τ_i is the corresponding path delay. Note that path delays greater than the inverse of the signal bandwidth are excluded from the CIR since their effect will be negligible on the LOS component. The CIR can be used to measure the effect of multipath interference on the receiver's

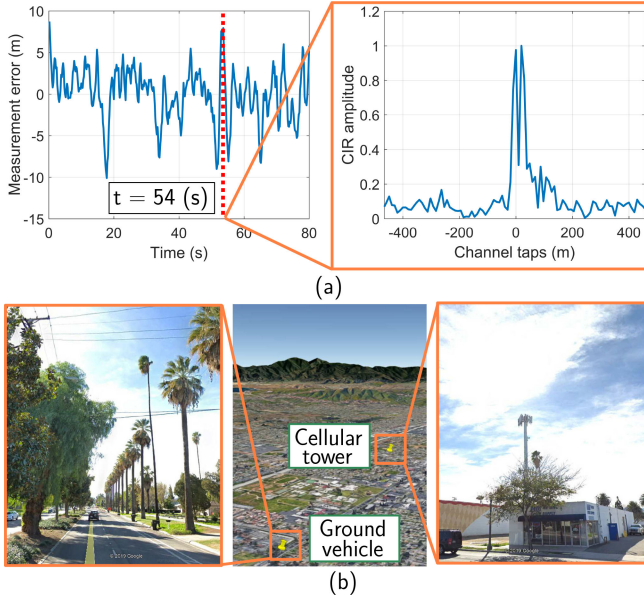


Fig. 5. (a): The measurement error and an estimated CIR at a particular time instance ($t = 45$ s) during which multipath exhibited a high amplitude. (b) The location of the cellular transmitter and the ground vehicle within the environment map.

delay-locked loop (DLL), denoted $\chi_n \triangleq \chi_{1,n}(i) + \chi_{2,n}(i)$, for $n = 1, \dots, N_s$, where $\chi_{1,n}(i)$ and $\chi_{2,n}(i)$ are functions of the subcarrier interval T_s , the DLL correlator spacing ξ , the number of subcarrier symbols in the LTE pilot signal M , the signal power due to antenna gain and implementation loss A , and the normalized symbol timing error \tilde{e}_θ . The detailed derivations of $\chi_{1,n}(i)$ and $\chi_{2,n}(i)$ is provided in [48]. The resulting induced multipath bias can be calculated according to

$$b_n = c \frac{\chi_n}{\kappa}, \quad \kappa \triangleq \frac{4\pi A \cos(\frac{\pi}{2^M})}{M [\sin(\frac{\pi}{2^M})]^3}, \quad (10)$$

where $M \triangleq \lfloor \frac{N_r}{6} \rfloor$, N_r denotes the number of subcarriers in the received LTE signal, and $\lfloor \cdot \rfloor$ denotes the integer floor function.

Fig. 5 shows the pseudorange measurement error and an instance of the estimated CIR from real LTE signals in an urban environment where the signals experience multipath. It can be seen that the power of the LOS component and that of the multipath component are comparable.

C. Outlier Detection and Exclusion

This subsection formulates the autonomous outlier detection and exclusion approach. Several methods to perform outlier detection have been proposed in the literature. This paper considers a classical RAIM-based outlier detection [49], which aims to detect large biases induced into the measurements due to LOS signal blockage. For complicated wireless environments, more sophisticated methods must be employed. Formulating other types of RAIM for SOP-GPS framework is similar and has been investigated in other work for GPS-SOP advanced-RAIM). In this work, it is assumed that only one measurement outlier exists. In the presence of a measurement bias due to LOS signal

blockage discussed in Section III-B1 or due to short multipath delays discussed in Section III-B2, a bias with magnitude f_n is injected in the pseudorange measurement drawn from the n -th cellular transmitter, rendering that particular measurement an outlier. In order to distinguish between outlier-free measurements and those subject to outliers, a measurable scalar parameter is defined that provides information about pseudorange measurement errors. This parameter, called a test statistic, is a random variable with a known distribution. Weighted least squares (WLS)-based filters, which use a weighted sum squared error (WSSE)-based test statistic have been demonstrated to result in an acceptable performance [50]. However, in [49], it was shown that using the normalized innovation squared (NIS)-based test statistic in an EKF-based framework was more robust against outliers compared to the WSSE-based test statistic in specific applications (e.g., railway navigation). In this paper, the NIS is used for generating the test statistic. The NIS-based test is formulated next.

Under outlier-free, normal operation, the innovation vector $\nu_0(k+1)$ and its associated innovation covariance $\mathbf{S}(k+1)$ are given by

$$\begin{aligned} \nu_0(k+1) &\triangleq z(k+1) - \hat{z}(k+1|j), \\ &\approx \mathbf{H}(k+1)\tilde{x}(k+1|j) + v'_s(k+1), \\ \mathbf{S}(k+1) &\triangleq \mathbf{H}(k+1)\mathbf{P}(k+1|j)\mathbf{H}^\top(k+1) + \mathbf{R}, \end{aligned} \quad (11)$$

where $v'_s \triangleq [v'_{s_1}, \dots, v'_{s_{N_s}}]^\top$. Whenever the n -th measurement experiences a bias, the biased innovation vector $\bar{\nu}(k+1)$ may be expressed as

$$\bar{\nu}(k+1) = \nu_0(k+1) + u_n(k+1),$$

where the vector $u_n(k+1) \triangleq [0, \dots, 0, f_n(k+1), 0, \dots, 0]^\top$ is the bias vector that results when a bias of magnitude f_n is present in the pseudorange measurement drawn from the outlier cellular tower. Note that $\bar{\nu}(k+1)$ has the same covariance as $\nu_0(k+1)$.

Denote $\nu(k+1)$ as the innovation vector evaluated by the EKF. Subsequently, the following hypotheses may be posed:

- Null hypothesis:

$$H_0 : \nu(k+1) = \nu_0(k+1).$$

- Alternative hypothesis:

$$H_1 : \nu(k+1) = \bar{\nu}(k+1).$$

The hypothesis test relies on the NIS-based test statistic, which is defined as

$$\varphi(k+1) \triangleq \nu^\top(k+1)\mathbf{S}^{-1}(k+1)\nu(k+1).$$

It is important to note that the NIS-based test statistics follows a chi-squared distribution under H_0 (outlier-free operation) and a non-central chi-squared distribution under H_1 (in the presence of outliers) [50]. Both distributions under H_0 and H_1 have the same degrees of freedom $d = N_s$. The non-centrality parameter under H_1 (in the presence of outliers) is given by

$$\lambda(k+1) = u_n^\top(k+1)\mathbf{S}^{-1}(k+1)u_n(k+1).$$

Algorithm 1: Autonomous Measurement Outlier Detection and Exclusion.

Input: $N_s, T_h, \{z_{s_n}(k+1)\}_{n=1}^{N_s}, \nu(k+1)$, and $\mathbf{S}^{-1}(k+1)$
Output: $\{z_{s_n}(k+1)\}_{n=1}^{N_d}$, where $N_d \in \{N_s, N_s - 1\}$

- 1: Set $i = 1$
- 2: Set $\varphi(k+1) = \nu^T(k+1)\mathbf{S}^{-1}(k+1)\nu(k+1)$
- 3: If $\varphi(k+1) > T_h$
- 4: Exclude z_{s_i} from $\{z_{s_n}(k+1)\}_{n=1}^{N_s}$
- 5: Set $\varphi(k+1) = \nu^T(k+1)\mathbf{S}^{-1}(k+1)\nu(k+1)$
- 6: If $\varphi(k+1) \leq T_h$
- 7: Add z_{s_i} to $\{z_{s_n}(k+1)\}_{n=1}^{N_s-1}$
- 8: Set $i = i + 1$
- 9: If $i \leq N_s$
- 10: Go to Step 4
- 11: Else
- 12: RAIM is not available: there is an outlier, but it cannot be detected
- 13: Exit Algorithm
- 14: End if
- 15: Else
- 16: *i*-th measurement is declared as an outlier
- 17: Feed navigation block with $\{z_{s_n}(k+1)\}_{n=1}^{N_s} - \setminus \{z_{s_i}(k+1)\}$
- 18: Exit Algorithm
- 19: End if
- 20: Else,
- 21: No outlier is detected
- 22: Feed navigation block with $\{z_{s_n}(k+1)\}_{n=1}^{N_s}$
- 23: Exit Algorithm
- 24: End if

Outlier detection is achieved by comparing the test statistic against a detection threshold T_h , namely

$$\begin{aligned}\varphi(k+1) \leq T_h : H_0 &\text{ is accepted (no outliers present),} \\ \varphi(k+1) > T_h : H_1 &\text{ is accepted (outlier present),}\end{aligned}$$

where a Neyman-Pearson approach is taken to obtain T_h given a desired probability of false alarm P_{FA} according to

$$P_{FA} = \int_{T_h}^{\infty} f_{\chi_d^2}(\tau) d\tau, \quad (12)$$

where $f_{\chi_d^2}$ represents the pdf of the test statistic under H_0 , specifically chi-squared distribution with d degrees of freedom.

Once a desired P_{FA} is fixed, T_h can be evaluated numerically from (12) or via chi-squared cumulative density function (cdf) table. Once an outlier is detected, its measurement is excluded from the measurement set and the EKF measurement update is subsequently performed without this measurement. The autonomous measurement outlier detection and exclusion algorithm is summarized in Algorithm 1.

IV. EXPERIMENTAL RESULTS

A field test with real LTE signals was performed to validate the efficacy and accuracy of the proposed outlier detection and exclusion approach. In this section, the experimental setup and experimental scenario description are first presented. Then, the corresponding results are shown.

A. Experimental Hardware Setup and Scenario Description

A vehicle was equipped with following hardware and software setup:

- A Septentrio AsteRx-i V integrated GNSS-IMU whose x -axis points toward the front of the vehicle, z -axis points upward, and y -axis points to the right side of the car. AsteRx-i V is equipped with a dual-antenna, multi-frequency GNSS receiver and a Vectornav VN-100 micro-electromechanical system (MEMS) IMU. The raw measurements from the IMU was used for the EKF time update step described in Section II-B at a rate of 100 Hz.
- Septentrio's post-processing software development kit (PP-SDK) was used to process carrier phase observables collected by the AsteRx-i V and by a nearby differential GPS base station to obtain a carrier phase-based navigation solution. This integrated GNSS-IMU real-time kinematic (RTK) system [51] was used to produce the ground truth results with which the proposed navigation framework was compared.
- Two cellular antennas to acquire and track signals from nearby cellular LTE towers. The LTE antennas used for the experiment were consumer-grade 800/1900 MHz cellular antennas [52]. The signals were simultaneously down-mixed and synchronously sampled at 10 mega-samples per second (MSPS) via a National Instruments (NI) dual-channel universal software radio peripheral (USRP)-2954R, driven by a GPSDO [53]. These samples were then processed by MATRIX SDR [15], [20], [21], developed by the Autonomous Systems Perception, Intelligence, and Navigation (ASPIN) Laboratory at the University of California, Irvine.

A stationary base receiver with the knowledge of its own location was also deployed in the same cellular environment of the navigating vehicle and was equipped with the following hardware setup:

- Two consumer-grade 800/1900 MHz cellular antennas.
- Two NI USRP-2920 which were synchronized via a multiple-input and multiple-output (MIMO) cable.

The clock bias and drift process noise power spectral densities of the receiver were set to be 1.3×10^{-22} s and 7.89×10^{-25} 1/s respectively, since the 2954R USRP was equipped with OCXO. The receiver was tuned to carrier frequencies of 1955 MHz and 739 MHz, which are channels allocated for U.S. cellular provider AT&T. Samples of the received signals were stored for off-line post-processing. The SDR developed in [20] was used to produce LTE pseudoranges.

Fig. 6 illustrates the experimental hardware setup, experimental environment, and traversed trajectory along with the



Fig. 6. (a) Environment layout showing the vehicle’s traversed trajectory (and a zoom on the streets where the vehicle drove), the base’s location, and the locations of the five LTE towers from which pseudorange measurements were received. Also shown are the navigation solutions without the measurement exclusion and with the measurement exclusion (proposed framework). (b) Experimental hardware setup.

position of the base and cellular towers. The initial estimates of the vehicle’s orientation ${}^L\hat{\mathbf{q}}(0| - 1)$, position ${}^G\hat{\mathbf{r}}_r(0| - 1)$, and velocity ${}^G\dot{\hat{\mathbf{r}}}_r(0| - 1)$, and their covariances were initialized using the output of the GNSS-IMU system. The initial estimates of the gyroscope’s and accelerometer’s biases; $\hat{\mathbf{b}}_g(0| - 1)$ and $\hat{\mathbf{b}}_a(0| - 1)$, respectively; were obtained by averaging 5 seconds of IMU measurements at a sampling period of $T = 0.01$ seconds, while the vehicle was stationary. Since the vehicle had initial access to GNSS signals, the initial value of the vehicle-mounted receiver’s clock error states $\hat{\mathbf{x}}_{\text{clk},r}(0| - 1)$ was obtained. The initial uncertainties associated with these state estimates were set to $\mathbf{P}_{L\hat{\mathbf{q}}}(0| - 1) = (1 \times 10^{-3})\mathbf{I}_{3 \times 3}$, $\mathbf{P}_{G\mathbf{r}_r}(0| - 1) = \text{diag}[10, 10, 0]$, $\mathbf{P}_{G\dot{\mathbf{r}}_r}(0| - 1) = \text{diag}[0.5, 0.5, 0]$, $\mathbf{P}_{\mathbf{b}_g}(0| - 1) = (3.75 \times 10^{-9})\mathbf{I}_{3 \times 3}$, $\mathbf{P}_{\mathbf{b}_a}(0| - 1) = (9.6 \times 10^{-5})\mathbf{I}_{3 \times 3}$, and $\mathbf{P}_{\mathbf{x}_{\text{clk},r}}(0| - 1) = \text{diag}[3, 0.3]$, where $\text{diag}(\cdot)$ denote a diagonal matrix.

The probability of false alarm for the outlier detection test was set to $P_{\text{FA}} = 0.005$. The measurement noise variances were calculated empirically while the vehicle had access to GNSS signals according to

$$\sigma_{v,s_n}^2 \approx \frac{1}{k_{\text{cutoff}} - 1} \sum_{k=0}^{k_{\text{cutoff}}-1} \hat{v}_{s_n}^2(k),$$

TABLE III
LTE TOWERS’ CHARACTERISTICS

eNodeB	Carrier frequency (MHz)	Cell ID	Bandwidth (MHz)
1	1955	216	20
2	739	319	10
3	739	288	10
4	739	151	10
5	739	232	10

where k_{cutoff} is the time-step at which GNSS signals were cut off and

$$\begin{aligned} \hat{v}'_{s_n}(k) &\triangleq z_{s_n}(k) - \|{}^G\mathbf{r}_{r,\text{GNSS}}(k) - \mathbf{r}_{s_n}\|_2 \\ &- c [\delta t_{r,\text{GNSS}}(k) - \hat{\delta t}_{s_n}(k|k)], \end{aligned} \quad (13)$$

where ${}^G\mathbf{r}_{r,\text{GNSS}}$ and $\delta t_{r,\text{GNSS}}$ are the vehicle-mounted receiver’s position and clock bias estimates obtained using GNSS signals and $\hat{\delta t}_{s_n}$ is the clock bias estimate produced by the base.

Over the course of the experiment, the receiver was listening to 5 LTE towers with the characteristics shown in Table III.

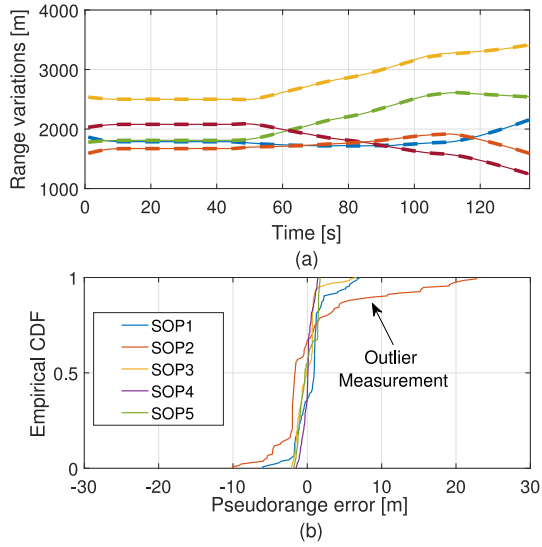


Fig. 7. 0.8(a) LTE pseudorange (solid lines) and true range (dashed lines) variations and (b) empirical cdf of the LTE pseudoranges for towers 1–5, respectively.

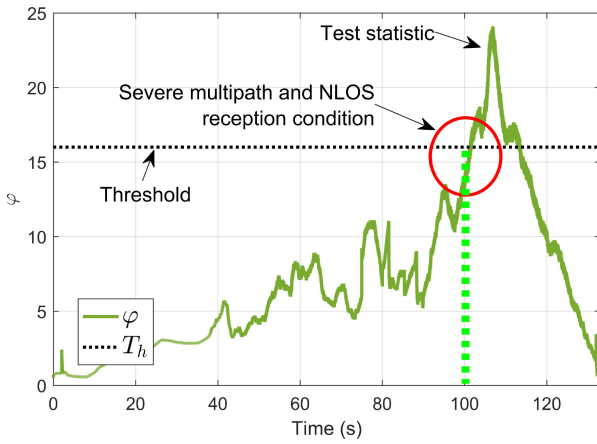


Fig. 8. The resulting outlier detection test which compares the test statistic φ against the detection threshold T_h .

In this experiment, the receiver traversed a trajectory of 1500 m over 135 s in an urban environment (downtown Riverside, California, U.S.). As can be seen from Fig. 6, the traversed path was surrounded by tall trees and the received signal experienced severe attenuation effect. Fig. 7(a) shows the LTE pseudorange (solid lines) and the true range (dashed lines) variations and Fig. 7(b) shows the empirical cdf of the LTE pseudorange measurement errors. The true ranges are known from the knowledge of the transmitters' location and the receiver's ground truth position, which was obtained from the integrated GNSS-IMU RTK system.

B. Experimental Results

The outlier detection and exclusion approach was applied throughout the vehicle's traversed trajectory. Fig. 8 shows the outlier detection test, which compares the test statistic φ against

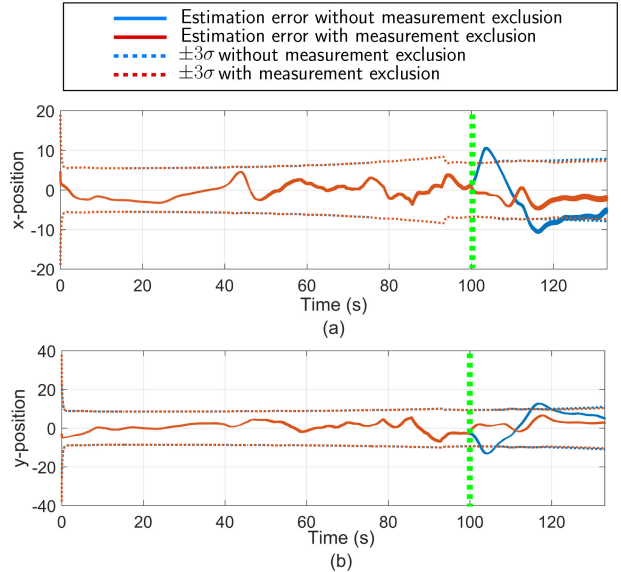


Fig. 9. The resulting position estimation errors and corresponding $\pm 3\sigma$ bounds with and without using the proposed outlier exclusion.

TABLE IV
NAVIGATION PERFORMANCE WITH AND WITHOUT OUTLIER DETECTION AND EXCLUSION

Method	2-D RMSE [m]	2-D Max. error [m]
Without measurement exclusion	8.2	20.4
With measurement exclusion	4.8	11.6
Reduction	41.46%	43.14%

the detection threshold T_h . It can be seen that at $t = 100$ s, the threshold is exceeded; therefore, the test is not declared successful (see the red circle in Fig. 8). This implies that at least one of the measurements was detected as an outlier and its contribution to the test statistic was significant enough for the detection algorithm to trigger.

In this experiment, the outlier exclusion technique indicated that the outlier measurement was the pseudorange drawn from the second cellular tower. Fig. 9(a)–(b) shows the resulting position estimation error and corresponding $\pm 3\sigma$ bounds with and without using the proposed outlier exclusion. As can be seen, outlier exclusion results in a significant reduction in the x - and y -position estimation error.

The pdf of the test statistic as calculated from the experimental data is plotted in Fig. 10 for the (a) outlier-free case (i.e., after the outlier was detected and excluded) and (b) in the presence of outlier (i.e., before it was detected and excluded). Overlaid on each pdf is an analytical pdf of (a) central chi-squared distribution with $d = 5$ and (b) non-central chi-squared distribution with $d = 5$ and $\lambda = 12$. It can be seen that the empirical pdfs follow the analytical pdfs.

Table IV compares the navigation performance of the proposed framework versus that of the navigation solution without

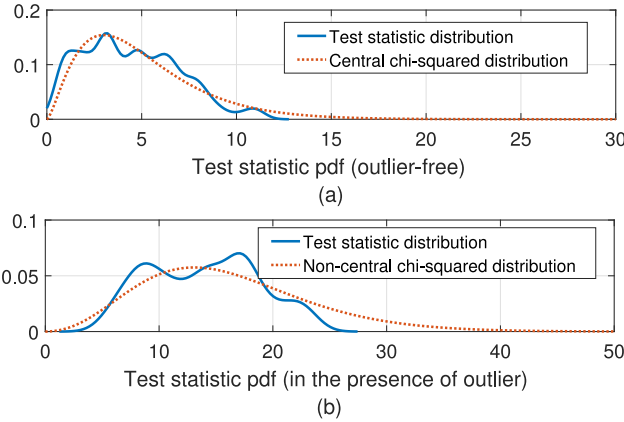


Fig. 10. The resulting probability distribution of the test statistic. (a): The test statistic distribution in outlier-free and (b) the test statistic distribution in the presence of outlier operation. It is evident that the test statistic follows closely the central and non-central chi-squared distributions in the outlier-free and in the presence of the outlier, respectively.

outlier exclusion. It can be noted from Fig. 9 and Table IV, not only the outlier detection and exclusion reduced the estimation error, it also resulted in estimation error consistent with the $\pm 3\sigma$ bounds.

V. CONCLUSION

In this paper, a framework for ground vehicle outlier detection and exclusion in GNSS-denied environment was developed. To this end, an EKF-based navigation framework was proposed which used IMU data and pseudoranges extracted from ambient cellular LTE towers. This paper characterized LTE pseudorange measurements from an extensive wardriving campaign collected with a ground vehicle in different environments: open sky, urban, and deep urban. Also, it characterized LOS blockage and short multipath delays. Next, an autonomous outlier detection and exclusion framework was formulated and evaluated using realistic experimental test. The results validated the efficacy of the proposed framework on a ground vehicle navigating in a deep urban environment over trajectory of 1500 m in the absence of GNSS signals. The results showed that the proposed technique reduces the position 2-D RMSE by 41.5% and the maximum position error by 43.1%.

APPENDIX A

VEHICLE KINEMATICS MODEL AND EKF TIME UPDATE

The IMU produces noisy measurements of angular rotation ${}^I\omega_r$ and linear acceleration ${}^G\dot{r}_r$, corrupted by the gyroscope and accelerometer biases, respectively. The IMU samples the angular rate ω_{meas} and specific forces a_{meas} every T seconds and can be modeled as

$$\omega_{\text{meas}}(k) = {}^I\omega_r(k) + b_g(k) + n_g(k),$$

$$a_{\text{meas}}(k) = \mathbf{R} \left[{}^I_G \bar{q} \right] [{}^G a_r(k) - {}^G g(k)] + b_a(k) + n_a(k),$$

where I_k is the inertial frame at time-step k , $\mathbf{R}[\bar{q}]$ is the equivalent rotation matrix of \bar{q} , ${}^G g$ is the acceleration due to gravity in

the global frame, and n_g and n_a are measurement noise vectors, which are modeled as zero-mean white noise sequences with covariances $\sigma_g^2 \mathbf{I}_{3 \times 3}$ and $\sigma_a^2 \mathbf{I}_{3 \times 3}$, respectively. The orientation of the IMU evolves according to

$${}^{I_{k+1}}_G \bar{q} = {}^{I_{k+1}}_k \bar{q} \otimes {}^I_{I_k} \bar{q}, \quad (14)$$

where \otimes is the quaternion multiplication operator and ${}^{I_{k+1}}_k \bar{q}$ represents the relative rotation of the inertial frame from time-step k to $k+1$, which is the solution to the differential equation

$${}^{I_k}_k \dot{\bar{q}} = \frac{1}{2} \Omega [{}^I \omega_r(\tau)] {}^{I_k}_k \bar{q}, \quad \tau \in [t_k, t_{k+1}], \quad (15)$$

where $t_k \triangleq kT$ and for any vector $\omega \triangleq [\omega_1, \omega_2, \omega_3]^T \in \mathbb{R}^3$, the matrix $\Omega[\omega]$ is defined as

$$\Omega[\omega] \triangleq \begin{bmatrix} -[\omega \times] & \omega \\ -\omega^T & 0 \end{bmatrix}, \quad [\omega \times] \triangleq \begin{bmatrix} 0 & \omega_3 & -\omega_2 \\ -\omega_3 & 0 & \omega_1 \\ \omega_2 & -\omega_1 & 0 \end{bmatrix}. \quad (16)$$

The biases b_g and b_a , the velocity, and the position evolve according to

$$\dot{b}_g = w_g, \quad \dot{b}_a = w_a, \quad (17)$$

$${}^G \dot{r}_r(k+1) = {}^G \dot{r}_r(k) + \int_{t_k}^{t_{k+1}} {}^G a_r(\tau) d\tau, \quad (18)$$

$${}^G r_r(k+1) = {}^G r_r(k) + \int_{t_k}^{t_{k+1}} {}^G \dot{r}_r(\tau) d\tau, \quad (19)$$

where w_g and w_a are modeled as zero-mean white random processes with covariances $\sigma_{w_g}^2 \mathbf{I}_{3 \times 3}$ and $\sigma_{w_a}^2 \mathbf{I}_{3 \times 3}$, respectively. Additional details of the orientation, position, and velocity models are discussed in [39], [54]. Given the model (17), the EKF time update can be readily calculated to yield $\hat{b}_g(k+1|j)$ and $\hat{b}_a(k+1|j)$, for $j \leq k$, according to

$$\hat{b}_g(k+1|j) = \hat{b}_g(k|j), \quad \hat{b}_a(k+1|j) = \hat{b}_a(k|j). \quad (20)$$

The orientation state estimate propagation equation is given by [39]

$${}^{I_{k+1}|j} \hat{q} = {}^{I_{k+1}} \hat{q} \otimes {}^{I_{k|j}} \hat{q}, \quad (21)$$

where ${}^{I_{k+1}} \hat{q}$ represents the estimated relative rotation of the vehicle from time-step k to $k+1$. The expression of ${}^{I_{k+1}} \hat{q}$ can be found in [39]. The vehicle's velocity state estimate time update equation is obtained using trapezoidal integration and is given by [39]

$$\begin{aligned} {}^G \hat{r}_r(k+1|j) = & {}^G \hat{r}_r(k|j) + \frac{T}{2} [\hat{s}(k|j) \\ & + \hat{s}(k+1|j)] + T {}^G g(k), \end{aligned} \quad (22)$$

where $\hat{s}(k|j) \triangleq \mathbf{R}_{\hat{q}}^T(k|j) \hat{a}(k|j)$, $\hat{a}(k|j) \triangleq a_{\text{meas}}(k) - \hat{b}_a(k|j)$, $\mathbf{R}_{\hat{q}}(k|j) \triangleq \mathbf{R}[{}^{I_{k|j}} \hat{q}]$, and ${}^G g(k)$ is the acceleration due to gravity in the global frame. The vehicle's position state

estimate time update is given by [39]

$${}^G\hat{\mathbf{r}}_r(k+1|j) = {}^G\hat{\mathbf{r}}_r(k|j) + \frac{T}{2} \left[{}^G\hat{\mathbf{r}}_r(k+1|j) + {}^G\hat{\mathbf{r}}_r(k|j) \right]. \quad (23)$$

APPENDIX B EKF PREDICTION ERROR COVARIANCE TIME UPDATE

Sections II-A and II-B described how to obtain the EKF state estimate time update for the vehicle-mounted receiver clock errors and vehicle's quaternion, position, velocity, gyroscope bias, and accelerometer bias. This subsection discusses calculation of the prediction error covariance time update. The EKF estimates the state vector \mathbf{x} consisting of the vehicle's and the receiver's clock error states, i.e., $\mathbf{x} \triangleq [\mathbf{x}_v^\top, \mathbf{x}_{\text{clk},r}^\top]^\top$. Denote

$$\begin{aligned} \hat{\mathbf{x}}(k|j) &\triangleq \begin{bmatrix} {}^{I_{k|j}}\hat{\mathbf{q}}^\top, {}^G\hat{\mathbf{r}}_r^\top(k|j), {}^G\hat{\mathbf{r}}_r^\top(k|j), \\ \hat{\mathbf{b}}_g^\top(k|j), \hat{\mathbf{b}}_a^\top(k|j), \hat{\mathbf{x}}_{\text{clk},r}^\top(k|j) \end{bmatrix}^\top, \end{aligned}$$

the state estimate produced by the EKF at time-step k obtained using all measurements (IMU and cellular pseudorange) from time-step 1 to $j \leq k$. Subsequently, the EKF prediction error covariance time update is given by

$$\mathbf{P}(k+1|j) = \mathbf{F}\mathbf{P}(k|j)\mathbf{F}^\top + \mathbf{Q}, \quad (24)$$

$$\mathbf{F} \triangleq \text{diag}[\Phi_r, \Phi_{\text{clk},r}], \quad \mathbf{Q} \triangleq \text{diag}[\mathbf{Q}_r, \mathbf{Q}_{\text{clk},r}],$$

$$\begin{aligned} \Phi_r &= \begin{bmatrix} \mathbf{I}_{3 \times 3} & \mathbf{0}_{3 \times 3} & \mathbf{0}_{3 \times 3} & \Phi_{qb_g} & \Phi_{qb_a} \\ \Phi_{rq} & \mathbf{I}_{3 \times 3} & \mathbf{I}_{3 \times 3}T & \Phi_{rb_g} & \Phi_{rb_a} \\ \Phi_{\dot{r}q} & \mathbf{0}_{3 \times 3} & \mathbf{I}_{3 \times 3} & \Phi_{\dot{r}b_g} & \Phi_{\dot{r}b_a} \\ \mathbf{0}_{3 \times 3} & \mathbf{0}_{3 \times 3} & \mathbf{0}_{3 \times 3} & \mathbf{I}_{3 \times 3} & \mathbf{0}_{3 \times 3} \\ \mathbf{0}_{3 \times 3} & \mathbf{0}_{3 \times 3} & \mathbf{0}_{3 \times 3} & \mathbf{0}_{3 \times 3} & \mathbf{I}_{3 \times 3} \end{bmatrix}, \\ \Phi_{\dot{r}q} &= -\frac{T}{2} \lfloor [\hat{s}(k|j) + \hat{s}(k+1|j)] \times \rfloor, \quad \Phi_{rq} = \frac{T}{2} \Phi_{\dot{r}q}, \\ \Phi_{qb_g} &= -\frac{T}{2} [\mathbf{R}_{\hat{q}}^\top(k|j) + \mathbf{R}_{\hat{q}}^\top(k+1|j)], \quad \Phi_{qb_a} = -\Phi_{qb_g}, \\ \Phi_{\dot{r}b_g} &= -\frac{T}{2} \lfloor \hat{s}(k|j) \times \rfloor \Phi_{qb_g}, \quad \Phi_{\dot{r}b_a} = \Phi_{qb_g} + \Phi_{rb_g}, \\ \Phi_{rb_g} &= \frac{T}{2} \Phi_{\dot{r}b_g}, \quad \Phi_{rb_a} = \frac{T}{2} \Phi_{rb_a}, \quad \mathbf{Q}_r = \frac{T}{2} \Phi_v^\top \mathbf{N}_c \Phi_v + \mathbf{N}_c, \\ \mathbf{N}_c &= \text{diag} \left[\sigma_g^2 \mathbf{I}_{3 \times 3}, \mathbf{0}_{3 \times 3}, \sigma_a^2 \mathbf{I}_{3 \times 3}, \sigma_{w_g}^2 \mathbf{I}_{3 \times 3}, \sigma_{w_a}^2 \mathbf{I}_{3 \times 3} \right]. \end{aligned}$$

It is worth noting that a non-rotating global frame is assumed in the IMU measurement models. The detailed derivations of $\mathbf{P}(k|j)$, Φ_r , and \mathbf{Q}_r are described in [54], [55].

APPENDIX C DERIVATION OF EQUATION (9)

In this Appendix, the mismatch between the time evolution of true clock bias and its first-order polynomial approximation is analyzed and the error component due to this approximation,

i.e., η_{r,s_n} , is characterized. The first step is to estimate the constants initial clock bias $c\delta t_{r,s_n,0}$ and drift $c\dot{\delta}t_{r,s_n,0}$ and find the first-order polynomial approximation over all observations up to time-step $K-1$. It is important to note that the measurement noise will not be considered here as the mismatch between true clock bias and its first-order polynomial approximation is only affected by the process noise. Hence, the observation vector only includes the differences between the receiver's and transmitter's clock biases, i.e.,

$$\mathbf{y} \triangleq [c\Delta\delta t_{r,s_n}(0), \dots, c\Delta\delta t_{r,s_n}(K-1)]^\top. \quad (25)$$

A first-order polynomial can be fit to the observations using a least-squares estimator, which minimizes the cost function \mathbf{G} according to

$$\mathbf{G} = \left\| \mathbf{y} - \mathbf{S} \begin{bmatrix} c\dot{\delta}t_{r,s_n,0} \\ c\delta t_{r,s_n,0} \end{bmatrix} \right\|^2, \quad \mathbf{S} \triangleq \begin{bmatrix} 0 & T & \dots & (K-1)T \\ 1 & 1 & \dots & 1 \end{bmatrix}^\top,$$

over all possible $c\dot{\delta}t_{r,s_n,0}$ and $c\delta t_{r,s_n,0}$. The least-squares-based estimate of $c\delta t_{r,s_n,0}$ and $c\dot{\delta}t_{r,s_n,0}$ is given by

$$\begin{bmatrix} \widehat{c\dot{\delta}t}_{r,s_n,0} \\ \widehat{c\delta t}_{r,s_n,0} \end{bmatrix} = (\mathbf{S}^\top \mathbf{S})^{-1} \mathbf{S}^\top \mathbf{y},$$

and the mismatch error vector can be expressed as

$$\begin{aligned} \boldsymbol{\eta}_{r,s_n} &= \mathbf{y} - \mathbf{S} \begin{bmatrix} \widehat{c\dot{\delta}t}_{r,s_n,0} \\ \widehat{c\delta t}_{r,s_n,0} \end{bmatrix} \\ &= \mathbf{G}\mathbf{y}, \end{aligned} \quad (26)$$

where $\mathbf{G} = [\mathbf{I} - \mathbf{S}(\mathbf{S}^\top \mathbf{S})^{-1} \mathbf{S}^\top]$. Using (8), $c\Delta\delta t_{r,s_n}(k)$ can be expressed in the recursive form according to

$$\begin{aligned} c\Delta\delta t_{r,s_n}(k) &= c\Delta\delta t_{r,s_n}(0) + kTc\Delta\dot{\delta}t_{r,s_n}(0) \\ &\quad + \sum_{i=1}^{k-1} w_{\delta t_{r,s_n}}(i) + \sum_{i=1}^{k-2} (k-i-1)w_{\dot{\delta}t_{r,s_n}}(i). \end{aligned} \quad (27)$$

Substituting (27) into (25) results in

$$\mathbf{y} = \mathbf{S} \begin{bmatrix} c\Delta\delta t_{r,s_n}(0) \\ c\Delta\dot{\delta}t_{r,s_n}(0) \end{bmatrix} + \mathbf{F}_1 \mathbf{w}_1 + \mathbf{F}_2 \mathbf{w}_2, \quad (28)$$

where

$$\mathbf{F}_1 \triangleq \begin{bmatrix} 0 & 0 & \dots & 0 \\ 1 & 0 & \dots & 0 \\ \vdots & \vdots & \ddots & \vdots \\ 1 & 1 & \dots & 1 \end{bmatrix}_{(K) \times (K-1)},$$

$$\mathbf{F}_2 \triangleq \begin{bmatrix} 0 & 0 & \dots & 0 \\ 0 & 0 & \dots & 0 \\ T & 0 & \dots & 0 \\ 2T & T & \dots & 0 \\ \vdots & \vdots & \ddots & \vdots \\ (K-2)T & (K-3)T & \dots & T \end{bmatrix}_{(K) \times (K-2)},$$

and recall

$$\mathbf{w}_1 \triangleq [w_{\delta t_{r,s_n}}(0), \dots, w_{\delta t_{r,s_n}}(K-2)]^\top$$

$$\mathbf{w}_2 \triangleq [w_{\dot{\delta}t_{r,s_n}}(0), \dots, w_{\dot{\delta}t_{r,s_n}}(K-3)]^\top.$$

Substituting (28) into (26) yields

$$\boldsymbol{\eta}_{r,s_n} = \mathbf{GS} \begin{bmatrix} c\Delta\delta t_{r,s_n}(0) \\ c\Delta\dot{\delta}t_{r,s_n}(0) \end{bmatrix} + \mathbf{GF}_1 \mathbf{w}_1 + \mathbf{GF}_2 \mathbf{w}_2. \quad (29)$$

Since $\mathbf{GS} = 0$, (29) can be expressed as

$$\boldsymbol{\eta}_{r,s_n} = \mathbf{GF}_1 \mathbf{w}_1 + \mathbf{GF}_2 \mathbf{w}_2.$$

This shows that each element of $\boldsymbol{\eta}_{r,s_n}$ is a linear combination of $2K - 3$ zero-mean white noise, therefore, $\boldsymbol{\eta}_{r,s_n}$ is a zero-mean random vector with a covariance matrix given by

$$\begin{aligned} \mathbb{E}\{\boldsymbol{\eta}_{r,s_n} \boldsymbol{\eta}_{r,s_n}^\top\} &= \\ \mathbb{E}\{\mathbf{GF}_1 \mathbf{w}_1 \mathbf{w}_1^\top \mathbf{F}_1^\top \mathbf{G}^\top + \mathbf{GF}_2 \mathbf{w}_2 \mathbf{w}_2^\top \mathbf{F}_2^\top \mathbf{G}^\top \\ &\quad + \mathbf{GF}_1 \mathbf{w}_1 \mathbf{w}_2^\top \mathbf{F}_2^\top \mathbf{G}^\top + \mathbf{GF}_2 \mathbf{w}_2 \mathbf{w}_1^\top \mathbf{F}_1^\top \mathbf{G}^\top\} \\ &= q_{11} \mathbf{GF}_1 \mathbf{F}_1^\top \mathbf{G}^\top + q_{22} \mathbf{GF}_2 \mathbf{F}_2^\top \mathbf{G}^\top \\ &\quad + q_{12} \mathbf{G} \left\{ \mathbf{F}_1 \mathbf{H}_q \mathbf{F}_2^\top + \mathbf{F}_2 \mathbf{H}_q^\top \mathbf{F}_1^\top \right\} \mathbf{G}^\top, \end{aligned} \quad (30)$$

where $\mathbf{H}_q = [\mathbf{I}_{(K-2) \times (K-2)}, \mathbf{0}_{(K-2) \times 1}]^\top$ and q_{ij} is ij -th element of the matrix $\mathbf{Q}_{\text{clk},r,s_n}$.

Remark: By extending the expression of matrix \mathbf{G} as a function of k and T , it can be shown that \mathbf{G} is a bisymmetric matrix. The covariance matrix of $\boldsymbol{\eta}_{r,s_n}$ consists of three terms shown in (30). By constructing $\mathbf{F}_1 \mathbf{F}_1^\top$, $\mathbf{F}_2 \mathbf{F}_2^\top$, and $\mathbf{F}_1 \mathbf{H}_q \mathbf{F}_2^\top + \mathbf{F}_2 \mathbf{H}_q^\top \mathbf{F}_1^\top$, it can be shown that each of the three terms of the covariance matrix are also bisymmetric. As a result, the diagonal elements of the covariance matrix of $\boldsymbol{\eta}_{r,s_n}$ are symmetric, as it is evident from Fig. 2.

ACKNOWLEDGMENT

The authors would like to thank Joe Khalife and Kimia Shamaei for her help with the data collection.

REFERENCES

- [1] S. Ji, W. Chen, X. Ding, Y. Chen, C. Zhao, and C. Hu, "Potential benefits of GPS/GLONASS/GALILEO integration in an urban canyon – Hong Kong," *J. Navigation*, vol. 63, no. 4, pp. 681–693, Oct. 2010.
- [2] D. Borio, F. Dovis, H. Kuusniemi, and L. L. Presti, "Impact and detection of GNSS jammers on consumer grade satellite navigation receivers," *Proc. IEEE*, vol. 104, no. 6, pp. 1233–1245, Jun. 2016.
- [3] K. Takeyama, T. Machida, Y. Kojima, and N. Kubo, "Improvement of dead reckoning in urban areas through integration of low-cost multisensors," *IEEE Trans. Intell. Veh.*, vol. 2, no. 4, pp. 278–287, Dec. 2017.
- [4] M. Maaref, J. Khalife, and Z. Kassas, "Lane-level localization and mapping in GNSS-challenged environments by fusing lidar data and cellular pseudoranges," *IEEE Trans. Intell. Veh.*, vol. 4, no. 1, pp. 73–89, Mar. 2019.
- [5] J. Meguro, T. Murata, J. Takiguchi, Y. Amano, and T. Hashizume, "GPS multipath mitigation for urban area using omnidirectional infrared camera," *IEEE Trans. Intell. Transp. Syst.*, vol. 10, no. 1, pp. 22–30, Mar. 2009.
- [6] Z. Sjanic and F. Gustafsson, "Simultaneous navigation and synthetic aperture radar focusing," *IEEE Trans. Aerosp. Electron. Syst.*, vol. 51, no. 2, pp. 1253–1266, Apr. 2015.
- [7] J. Raquet and R. Martin, "Non-GNSS radio frequency navigation," in *Proc. IEEE Int. Conf. Acoust., Speech Signal Process.*, Mar. 2008, pp. 5308–5311.
- [8] L. Merry, R. Faragher, and S. Schedin, "Comparison of opportunistic signals for localisation," in *Proc. IFAC Symp. Intell. Auton. Veh.*, Sep. 2010, pp. 109–114.
- [9] Z. Kassas, "Collaborative opportunistic navigation," *IEEE Aerosp. Electron. Syst. Mag.*, vol. 28, no. 6, pp. 38–41, Jun. 2013.
- [10] J. McEllroy, "Navigation using signals of opportunity in the AM transmission band," Master's thesis, Dept. Aeronaut. Astronaut., Air Force Inst. Technol., Wright-Patterson Air Force Base, Ohio, USA, 2006.
- [11] S. Fang, J. Chen, H. Huang, and T. Lin, "Is FM a RF-based positioning solution in a metropolitan-scale environment? A probabilistic approach with radio measurements analysis," *IEEE Trans. Broadcast.*, vol. 55, no. 3, pp. 577–588, Sep. 2009.
- [12] P. Thevenon *et al.*, "Positioning using mobile TV based on the DVB-SH standard," *NAVIGATION, J. Inst. Navigation*, vol. 58, no. 2, pp. 71–90, 2011.
- [13] C. Yang, T. Nguyen, and E. Blasch, "Mobile positioning via fusion of mixed signals of opportunity," *IEEE Aerosp. Electron. Syst. Mag.*, vol. 29, no. 4, pp. 34–46, Apr. 2014.
- [14] C. Chen and W. Wu, "Three-dimensional positioning for LTE systems," *IEEE Trans. Veh. Technol.*, vol. 66, no. 4, pp. 3220–3234, Apr. 2017.
- [15] Z. Kassas, J. Khalife, K. Shamaei, and J. Morales, "I hear, therefore I know where I am: Compensating for GNSS limitations with cellular signals," *IEEE Signal Process. Mag.*, vol. 34, no. 5, pp. 111–124, Sep. 2017.
- [16] S. Fang and Y. Yang, "The impact of weather condition on radio-based distance estimation: A case study in GSM networks with mobile measurements," *IEEE Trans. Veh. Technol.*, vol. 65, no. 8, pp. 6444–6453, Aug. 2016.
- [17] Z. Kassas, J. Morales, and J. Khalife, "New-age satellite-based navigation – STAN: Simultaneous tracking and navigation with LEO satellite signals," *Inside GNSS Mag.*, vol. 14, no. 4, pp. 56–65, 2019.
- [18] C. Yang and T. Nguyen, "Tracking and relative positioning with mixed signals of opportunity," *NAVIGATION, J. Inst. Navigation*, vol. 62, no. 4, pp. 291–311, Dec. 2015.
- [19] M. Driusso, C. Marshall, M. Sabathy, F. Knutti, H. Mathis, and F. Babich, "Vehicular position tracking using LTE signals," *IEEE Trans. Veh. Technol.*, vol. 66, no. 4, pp. 3376–3391, Apr. 2017.
- [20] K. Shamaei, J. Khalife, and Z. Kassas, "Exploiting LTE signals for navigation: Theory to implementation," *IEEE Trans. Wireless Commun.*, vol. 17, no. 4, pp. 2173–2189, Apr. 2018.
- [21] K. Shamaei and Z. Kassas, "LTE receiver design and multipath analysis for navigation in urban environments," *NAVIGATION, J. Inst. Navigation*, vol. 65, no. 4, pp. 655–675, Dec. 2018.
- [22] K. Shamaei and Z. Kassas, "Sub-meter accurate UAV navigation and cycle slip detection with LTE carrier phase," in *Proc. ION GNSS Conf.*, Sep. 2019, pp. 2469–2479.
- [23] J. Khalife and Z. Kassas, "Precise UAV navigation with cellular carrier phase measurements," in *Proc. IEEE/ION Position, Location, Navigation Symp.*, Apr. 2018, pp. 978–989.
- [24] P. Enge, "Local area augmentation of GPS for the precision approach of aircraft," *Proc. IEEE*, vol. 87, no. 1, pp. 111–132, Jan. 1999.
- [25] H. Kuusniemi, A. Wieser, G. Lachapelle, and J. Takala, "User-level reliability monitoring in urban personal satellite-navigation," *IEEE Trans. Aerosp. Electron. Syst.*, vol. 43, no. 4, pp. 1305–1318, Oct. 2007.
- [26] K. Ansari, Y. Feng, and M. Tang, "A runtime integrity monitoring framework for real-time relative positioning systems based on GPS and DSRC," *IEEE Trans. Intell. Transp. Syst.*, vol. 16, no. 2, pp. 980–992, Apr. 2015.
- [27] M. Joerger and B. Pervan, "Fault detection and exclusion using solution separation and chi-squared ARAIM," *IEEE Trans. Aerosp. Electron. Syst.*, vol. 52, no. 2, pp. 726–742, Apr. 2016.
- [28] S. Khanafseh, N. Roshan, S. Langel, F. Chan, M. Joerger, and B. Pervan, "GPS spoofing detection using RAIM with INS coupling," in *Proc. IEEE/ION Position, Location, Navigation Symp.*, May 2014, pp. 1232–1239.
- [29] M. Maaref, J. Khalife, and Z. Kassas, "Integrity monitoring of LTE signal of opportunity-based navigation for autonomous ground vehicles," in *Proc. ION GNSS Conf.*, Sep. 2018, pp. 2456–2466.
- [30] J. Morales, P. Roysdon, and Z. Kassas, "Signals of opportunity aided inertial navigation," in *Proc. ION GNSS Conf.*, Sep. 2016, pp. 1492–1501.
- [31] Z. Kassas, J. Morales, K. Shamaei, and J. Khalife, "LTE steers UAV," *GPS World Mag.*, vol. 28, no. 4, pp. 18–25, Apr. 2017.
- [32] Z. Kassas, V. Ghadiok, and T. Humphreys, "Adaptive estimation of signals of opportunity," in *Proc. ION GNSS Conf.*, Sep. 2014, pp. 1679–1689.

- [33] J. Morales and Z. Kassas, "Optimal collaborative mapping of terrestrial transmitters: receiver placement and performance characterization," *IEEE Trans. Aerosp. Electron. Syst.*, vol. 54, no. 2, pp. 992–1007, Apr. 2018.
- [34] J. Barnes *et al.*, "Characterization of frequency stability," *IEEE Trans. Instrum. Meas.*, vol. 20, no. 2, pp. 105–120, May 1971.
- [35] Y. Bar-Shalom, X. Li, and T. Kirubarajan, *Estimation With Applications to Tracking and Navigation*. Hoboken, NJ, USA: Wiley, 2002.
- [36] A. Thompson, J. Moran, and G. Swenson, *Interferometry and Synthesis in Radio Astronomy*, 2nd ed., Hoboken, NJ, USA: Wiley, 2001.
- [37] J. del Peral-Rosado *et al.*, "Software-defined radio LTE positioning receiver towards future hybrid localization systems," in *Proc. Int. Commun. Satell. Syst. Conf.*, Oct. 2013, pp. 14–17.
- [38] Z. Kassas and T. Humphreys, "Observability analysis of collaborative opportunistic navigation with pseudorange measurements," *IEEE Trans. Intell. Transp. Syst.*, vol. 15, no. 1, pp. 260–273, Feb. 2014.
- [39] M. Shelley, "Monocular visual inertial odometry," Master's thesis, Dept. Comput. Sci., Technical Univ. Munich, Munich, Germany, 2014.
- [40] N. Zhu, J. Marais, D. Betaille, and M. Berbineau, "GNSS position integrity in urban environments: A review of literature," *IEEE Trans. Intell. Transp. Syst.*, vol. 19, no. 9, pp. 2762–2778, Sep. 2018.
- [41] N. Kbayer and M. Sahmoudi, "Performances analysis of GNSS NLOS bias correction in urban environment using a three-dimensional city model and GNSS simulator," *IEEE Trans. Aerosp. Electron. Syst.*, vol. 54, no. 4, pp. 1799–1814, Feb. 2018.
- [42] L. Heng, "Safe satellite navigation with multiple constellations: Global monitoring of GPS and GLONASS signal-in-space anomalies," Ph.D. dissertation, Dept. Elect. Eng., Stanford Univ., Stanford, CA, USA, 2012.
- [43] P. Misra and P. Enge, *Global Positioning System: Signals, Measurements, and Performance*, 2nd ed., Lincoln, MA, USA: Ganga-Jamuna Press, 2010.
- [44] D. Bladzio, M. Hogan, and S. Ruffini, "Synchronization aspects in LTE small cells," *IEEE Commun. Mag.*, vol. 51, no. 9, pp. 70–77, Sep. 2013.
- [45] F. Knutti, M. Sabathy, M. Driusso, H. Mathis, and C. Marshall, "Positioning using LTE signals," in *Proc. Navigation Conf. Eur.*, Apr. 2015, pp. 1–8.
- [46] W. Xu, M. Huang, C. Zhu, and A. Dammann, "Maximum likelihood TOA and OTDOA estimation with first arriving path detection for 3GPP LTE system," *Trans. Emerg. Telecommun. Technologies*, vol. 27, no. 3, pp. 339–356, 2016.
- [47] K. Shamaei, J. Khalife, and Z. Kassas, "Comparative results for positioning with secondary synchronization signal versus cell specific reference signal in LTE systems," in *Proc. ION Int. Tech. Meeting Conf.*, Jan. 2017, pp. 1256–1268.
- [48] B. Yang, K. Letaief, R. Cheng, and Z. Cao, "Timing recovery for OFDM transmission," *IEEE J. Sel. Areas Commun.*, vol. 18, no. 11, pp. 2278–2291, Nov. 2000.
- [49] A. Gorsch, O. Crespillo, I. Martini, and C. Gunther, "Snapshot residual and Kalman filter based fault detection and exclusion schemes for robust railway navigation," in *Proc. Eur. Navigation Conf.*, May 2017, pp. 36–47.
- [50] S. Bhattacharyya and D. Gebre-Egziabher, "Kalman filter-based RAIM for GNSS receivers," *IEEE Trans. Aerosp. Electron. Syst.*, vol. 51, no. 3, pp. 2444–2459, Jul. 2015.
- [51] "Septentrio AsteRx-i V," 2018. [Online]. Available: <https://www.septentrio.com/products>
- [52] "Laird phantom 3G/4G multiband antenna NMO mount white TRA6927M3NB," [Online]. Available: <https://www.lairdtech.com/products/phantom-series-antennas>
- [53] "National instrument universal software radio peripheral-2954r," [Online]. Available: <http://www.ni.com/en-us/support/model.usrp-2954.html>
- [54] P. Groves, *Principles of GNSS, Inertial, and Multisensor Integrated Navigation Systems*, 2nd ed., Norwood, MA, USA: Artech House, 2013.
- [55] J. Farrell and M. Barth, *The Global Positioning System and Inertial Navigation*. New York, NY, USA: McGraw-Hill, 1998.



Mahdi Maaref received a B.S. and M.S. from the University of Tehran in 2008 and 2011, respectively, and a Ph.D. in Electrical Engineering from Shahid Beheshti University, in 2016. He was a Visiting Research Collaborator at the University of Alberta, Edmonton, Canada in 2016. Currently, he is a postdoctoral Research Fellow at the University of California, Riverside and a member of the Autonomous Systems Perception Intelligent and Navigation (ASPIN) Laboratory. His research interests include autonomous ground vehicles, opportunistic perception, and autonomous integrity monitoring.



Zak (Zaher) M. Kassas (Senior Member, IEEE) is an assistant professor at the University of California, Irvine and director of the ASPIN Laboratory. He received a B.E. in Electrical Engineering from the Lebanese American University, an M.S. in Electrical and Computer Engineering from The Ohio State University, and an M.S.E. in Aerospace Engineering and a Ph.D. in Electrical and Computer Engineering from The University of Texas at Austin. In 2018, he received the National Science Foundation (NSF) Faculty Early Career Development Program (CAREER) award, and in 2019, he received the Office of Naval Research (ONR) Young Investigator Program (YIP) award. He is a recipient of 2018 IEEE Walter Fried Award, 2018 Institute of Navigation (ION) Samuel Burka Award, and 2019 ION Col. Thomas Thurlow Award. He is an Associate Editor for the IEEE TRANSACTIONS ON AEROSPACE AND ELECTRONIC SYSTEMS and the IEEE TRANSACTIONS ON INTELLIGENT TRANSPORTATION SYSTEMS. His research interests include cyber-physical systems, estimation theory, navigation systems, autonomous vehicles, and intelligent transportation systems.